Argonne NATIONAL LABORATORY

ANL/CFCT-25/18

Real-Time Characterization of Salt Aerosols Generated from Static and Sparged Molten Salt

Chemical and Fuel Cycle Technologies Division, Argonne National Laboratory

ANL/CFCT-25/18

Real-Time Characterization of Salt Aerosols Generated from Static and Sparged Molten Salts

Prepared by
Sara Thomas and Abbie O'Brien
Chemical and Fuel Cycle Technologies Division, Argonne National Laboratory

September 19, 2025

Acknowledgements

This report was produced under the auspices of the United States Department of Energy Office of Nuclear Energy Advanced Reactor Technologies Molten Salt Reactors Campaign. Issuance of this report meets milestone M3AT-25AN0702043.

This work was conducted at Argonne National Laboratory and supported by the U.S. Department of Energy, Office of Nuclear Energy, under Contract DE-AC02-06CH11357.

Table of Contents

Figures

Tables

Acronyms and Abbreviations

C_V	Volumetric particle concentration
D_{50}	Median diameter
dN/N	Fraction of total measured particles in a size bin
EDS	Energy-dispersive X-ray spectroscopy
HEPA filter	High efficiency particulate air filter
ICP-MS	Inductively coupled plasma-mass spectrometry
LBE	Licensing basis event
MFC	Mass flow controller
MSR	Molten salt reactor
MST	Mechanistic source term
NRC	Nuclear Regulatory Commission
P&ID	Process and instrumentation drawing
PSD	Particle size distribution
PTFE	Poly(tetrafluoroethylene)
SEM	Scanning electron microscopy
SLPM	Standard liters per minute

Abstract

The formation of radionuclide-bearing aerosols in the respirable size range has the potential to significantly influence offsite dose consequences and is, therefore, an important consideration in nuclear facility safety assessments. Molten salt reactor (MSR) developers will likely need to demonstrate an understanding of the conditions under which radionuclide-bearing aerosols may be generated from their reactor under normal operating and accident conditions, as well as the characteristics and transport behavior of these aerosols, to demonstrate to the U.S. Nuclear Regulatory Commission (NRC) that the facility can be operated safely. Recent reviews of the literature identified a lack of experimental data describing the mechanisms of formation and properties (size, concentration, and composition) of salt aerosol particles that are produced from molten salts. Experiments that identify the conditions that lead to radionuclide-bearing salt aerosol releases and quantify the characteristics of salt aerosols formed by different mechanisms are high-priority needs to support MSR licensing.

This report describes tests that were conducted within the Argonne Salt Aerosol Test Stand (a sealed vessel and measurement system) to generate salt aerosols from static and sparged molten salts and measure their size and concentration in real-time. The results provide insight into salt aerosol formation by the vapor condensation and bubble bursting mechanisms and inform the potential radiological consequences of aerosol formation from molten fuel salt. Videos of the salt surface were taken during salt sparge tests to observe surface bubble behavior. The data in this report can be used to develop mechanistic source term and accident progression models for MSRs. The real-time salt aerosol characterization technique used in this study will be employed in future integral effects tests that are conducted at an engineering scale to simulate realistic MSR accidents and in future separate effects tests to address additional variables that may impact salt aerosol characteristics (e.g., presence of fission products in salt and humidity in atmosphere).

1 Introduction

The U.S. Nuclear Regulatory Commission (NRC) issued Regulatory Guide 1.233 to provide advanced reactor developers a modernized licensing framework that is technology-inclusive, risk-informed, and performance-based. Within this framework, developers are directed to identify and evaluate licensing basis events (LBEs) that represent a broad range of postulated accident scenarios. LBEs are evaluated using accident progression models that simulate event sequences and assess potential outcomes and their safety significance. These simulations incorporate mechanistic source term (MST) models to predict radionuclide species formation and release by representing their expected physical and chemical behavior for the scenario under consideration. Both MST and accident progression models must be validated with experimental data.

A challenge that molten salt reactor (MSR) developers face in preparing U.S. NRC license applications is the lack of experimental data needed to quantify the safety consequences of postulated accident scenarios. One such knowledge gap is the limited availability of experimental data that assess the characteristics of salt aerosols that form from molten salt systems, and in particular, the identification of conditions that may lead to respirable and radionuclide-bearing salt aerosol releases (Gelbard et al., 2023; Shahbazi et al., 2022). Radionuclide-bearing aerosols are key contributors to the source term of a nuclear facility and can significantly impact MSR accident consequence. This is due to their tendency to remain airborne (increasing the likelihood of breaching containment barriers) and the significant radiological health risk posed by particles in the respirable size range. All MSR developers will likely evaluate the impact of an unintended release of molten fuel salt from the reactor vessel as an accident scenario in their licensing application. Experimental simulations of salt release accidents will therefore need to be conducted to generate datasets to validate accident progression models. These experimental accident simulations will require real-time measurements of salt aerosol size, concentration, and composition to track how particle characteristics evolve over the course of the accident.

The general goal of this project is to support MSR licensing and safety by generating experimental data that fill high-priority data gaps on safety-affecting processes for use in model development and validation. To meet this data need, Argonne has been developing methods to simulate processes significant to accident consequence for MSRs, developing techniques to quantify these processes, and conducting laboratory-scale tests to generate experimental data (Thomas and Jackson, 2021, 2022, 2023). Recent efforts have focused on developing the capability to measure the size and concentration of salt aerosols in real time (Thomas, 2024). An engineering-scale facility to simulate molten salt release accidents and to quantify the coupled radiological and thermohydraulic consequences at a scale suitable for validating systems-level codes (e.g., MELCOR) is currently being built at Argonne (Thomas, 2025).

This report presents real-time measurements of the size and concentration of salt aerosol particles generated from static and sparged molten salt. This work was performed using the Argonne Salt Aerosol Test Stand, which is a modular particle generation and measurement system developed to support separate effects testing and real-time characterization of salt aerosol particles produced under controlled conditions. The results generated from this test stand are designed to provide the mechanistic detail required to develop MST models on salt aerosol formation and transport. The quantitative accuracy of the particle size and concentration measurements under different atmospheres (i.e., air and argon) and the compatibility of the technique with corrosive and high-temperature salt environments were demonstrated during FY24 (Thomas, 2024). The experience gained through real-time salt aerosol measurements made using the Argonne Salt Aerosol Test Stand will be employed to characterize salt aerosols formed during accident simulations performed in the engineering-scale facility.

2 Argonne Salt Aerosol Test Stand description and methods

2.1 Salt aerosol generation from static and sparged salt

The Argonne Salt Aerosol Test Stand is a sealed vessel and measurement system that was designed to support the controlled generation and characterization of salt aerosol particles from molten salt under a variety of atmospheres and flow conditions. Figure 1 presents cutout section views of the vessel to illustrate how salt aerosols are generated by different mechanisms within the vessel. Specifically, salt particles can be formed by the condensation of vapors evolving from static molten salt (as depicted in Figure 1A) and by the mechanical breakup of bubbles at the salt surface during sparging with pre-heated argon gas (as depicted in Figure 1B). Salt is contained in a nickel crucible within the vessel for both aerosol generation approaches. The base of the vessel sits within a furnace, which heats the salt above the melting temperature under a flow of argon gas. During aerosol testing, a gas cylinder supplies a room temperature stream of gas that flows laterally into the headspace of the vessel and over the surface of the molten salt. The cooler lateral gas stream promotes the condensation of salt vapors that evolve from the molten salt. This gas stream also serves as the carrier gas to transport the generated salt aerosol particles to the aerosol sensor. For a static molten salt (no sparging), this system setup enables the analysis of salt aerosol formation by solely the vapor condensation mechanism (Figure 1A).

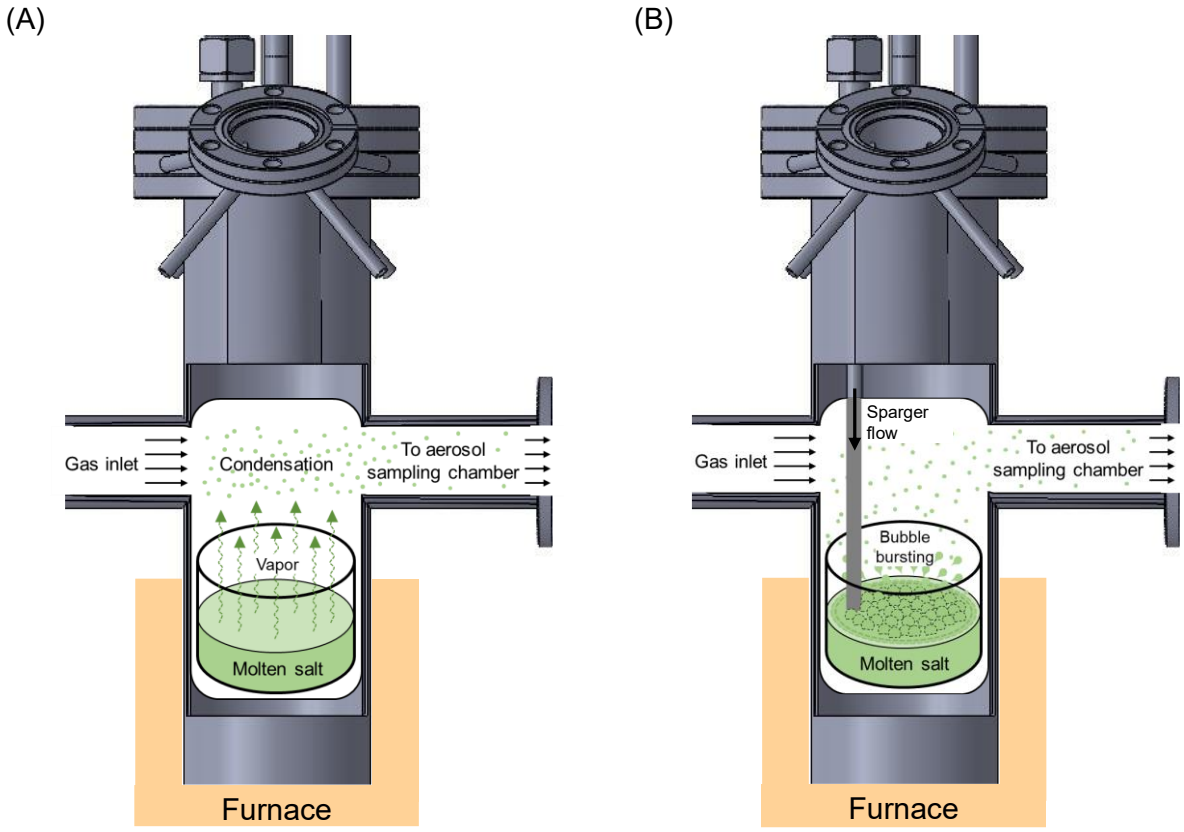

Figure 1: Section of aerosol generation vessel with schematic that depicts salt aerosol generation from (A) static and (B) sparged molten salt within the vessel interior.

Generating salt aerosols from sparged salt is accomplished by bubbling pre-heated gas into molten salt by using a custom sparging apparatus fed through the vessel lid (Figure 1B). The sparger is made of Type 316 stainless steel and channels gas through a porous metal disc to

produce a lateral distribution of bubbles that burst on the salt surface. An increase in the gas mass flow rate through the sparger should produce a proportionate increase in bubble formation and burst rate. Figure 2 presents side-view photographs of the sparger bubbling argon gas into a beaker of room-temperature water at different flow rates to show sparger operation and the effect of flow rate on the relative amount of bubbles formed.

0.05 L min^{-1} 0.2 L min^{-1} 0.5 L min^{-1}

Figure 2: Profile view of custom sparger bubbling argon gas into a beaker of water at flow rates of 0.05, 0.2 and 0.5 L min^{-1}.

For operation in molten salt, the sparger is immersed only for the testing duration to limit corrosion. In addition, the sparger is removed from the molten salt while gas is still flowing through the pores to prevent clogging. Salt aerosol measurements from static salt are taken prior to sparger immersion to provide a baseline measurement of particles formed without sparging under the same conditions.

2.2 Description of salt aerosol generation and measurement system

Figure 3 presents a drawing of the vessel and sampling chamber that were used to generate and sample salt aerosol particles, respectively. All components of the aerosol generation vessel and sampling chamber are made of Type 316 stainless steel. The base of the vessel was constructed from a seamless tube (12 in. long, 3 in. diameter) with a 3 in. diameter disc welded to one end. Gas flow channels (3.5 in. length, 1.5 in. diameter) protrude laterally from the vessel body, and viewport channels (8 in. length, 1.5 in. diameter) protrude from the vessel body at an angle. These channels are welded to the vessel body on one end and have flanges on the other end. The viewport channels are angled and capped with sapphire windows to enable observation of the interior of the vessel. The viewport channels contain a series of tubes that flow gas over the viewport windows to prevent the buildup of condensation from the salt contained within the vessel.

The aerosol sampling chamber is made from a seamless tube (12 in. long, 1.5 in. diameter) with flanges welded on both ends. The salt aerosol particles generated within the vessel are transported downstream to the aerosol sampling chamber, which serves multiple purposes:

- Cooling the particle-bearing carrier gas by increasing its residence time in the system prior to entering the sampling line (current sensor cuvette is rated to a temperature of 120 °C),
- Providing an outlet for the sampling line so the flow rate through the sampling line can be independent of the flow rate of the inlet gas, and
- Acting as a reservoir for generated particles that can be utilized in future tests, such as tests on particle aging and exposure to oxygen and humidity.

The aerosol sampling chamber incorporates ports for a pressure transducer and thermocouples to measure the pressure and temperature of the gas at the inlet of the sampling line, respectively (Figure 3). The vessel lid contains ports to evacuate and fill the vessel with gases, to feed the sparger into the molten salt contained within the vessel, and to feed thermocouples into the vessel.

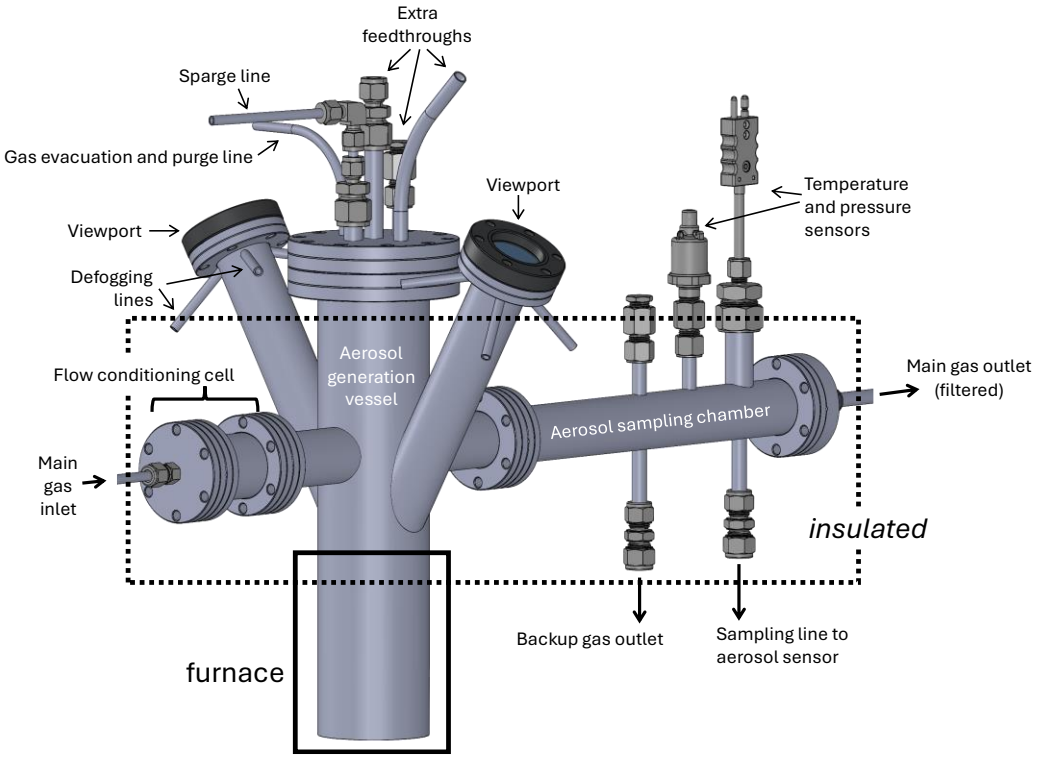

Figure 3: Drawing of salt aerosol generation vessel with aerosol sampling chamber.

The flow conditioning cell is located upstream of the aerosol generation vessel and is constructed from a seamless tube (3 in. long, 1.5 in diameter) with flanges on both ends. The interior of the cell contains a porous metal disc (316 stainless steel), mounted crosswise. The edges of the disc are welded to the inner walls. The porous metal disc equalizes the pressure and promotes orderly (laminar-like) flow of the inlet gas into the vessel, as shown in the schematic in Figure 4. The main gas inlet and main gas outlet tubing are connected to the flow conditioning cell and aerosol sampling chamber, respectively, with blind flange to tube fitting adapters. The lid, viewport windows, gas flow channels between the flow conditioning cell and vessel, gas flow channel between the vessel and aerosol sampling chamber, and blind flange to tube fitting adapters are joined with flanged connections.

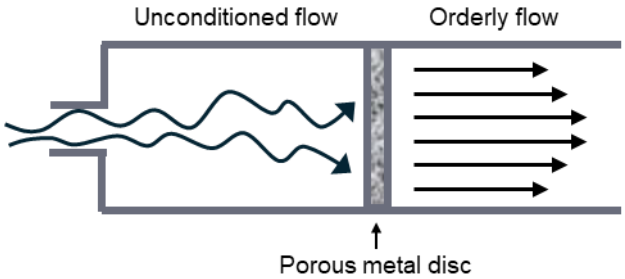

Figure 4: Schematic of the cross-section of the flow conditioning cell

An annotated picture of the Argonne Salt Aerosol Test Stand that was built inside a hood is shown in Figure 5. A simplified process and instrumentation drawing (P&ID) of the system is shown in Figure 6 to identify the multiple inlet and outlet gas lines. A gas cylinder supplies all the gas that flows into the system. Argon gas was used for the work presented in this report, but the system can accommodate other gas compositions. The salt aerosol generation and measurement system is fully isolated from the ambient atmosphere and vents into the hood through the main outlet and sampling lines when inlet gas is flowing into the system. Check valves are placed at the outlets of the main gas outlet and sampling lines to prevent backflow. The gas inlet line incorporates a mass flow controller (MFC) that regulates the flow of gas into the aerosol generation vessel (through the flow conditioning cell) to the desired rate (up to 20 standard liters per minute; SLPM). MFCs also regulate the flow of gas from the cylinder into the defogging lines and the sparge line. The sparge line gas is pre-heated by flowing gas through a copper coil within a furnace set to 250 °C.

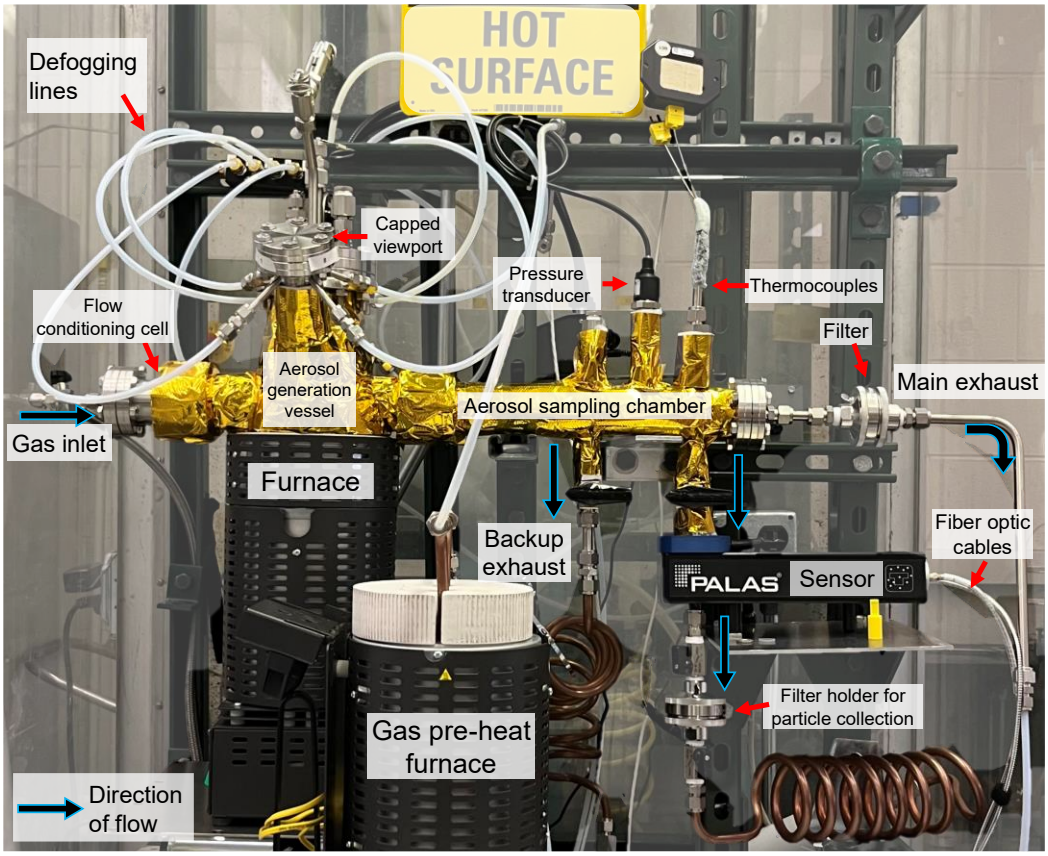

Figure 5: Annotated picture of the Argonne Salt Aerosol Test Stand in the hood to identify gas lines, gas line components, direction of flow, and system configuration.

The main gas outlet is always open when gas is flowing into the vessel and includes housing for a removable filter to collect salt aerosol particles, a copper coil, and a HEPA filter to filter and cool the exhaust. The sampling line that draws particle-bearing gas through the aerosol sensor cuvette includes a particle collection filter just downstream of the aerosol sensor, a copper coil for cooling, a HEPA filter, a MFC to regulate the gas mass flow rate, and a vacuum pump. The sampling line is opened when steady state conditions within the aerosol sampling chamber have been reached. The aerosol sampling chamber also incorporates a backup exhaust line that can be opened if the

main exhaust line becomes clogged with salt particles, as indicated by a pressure increase inside the aerosol sampling chamber.

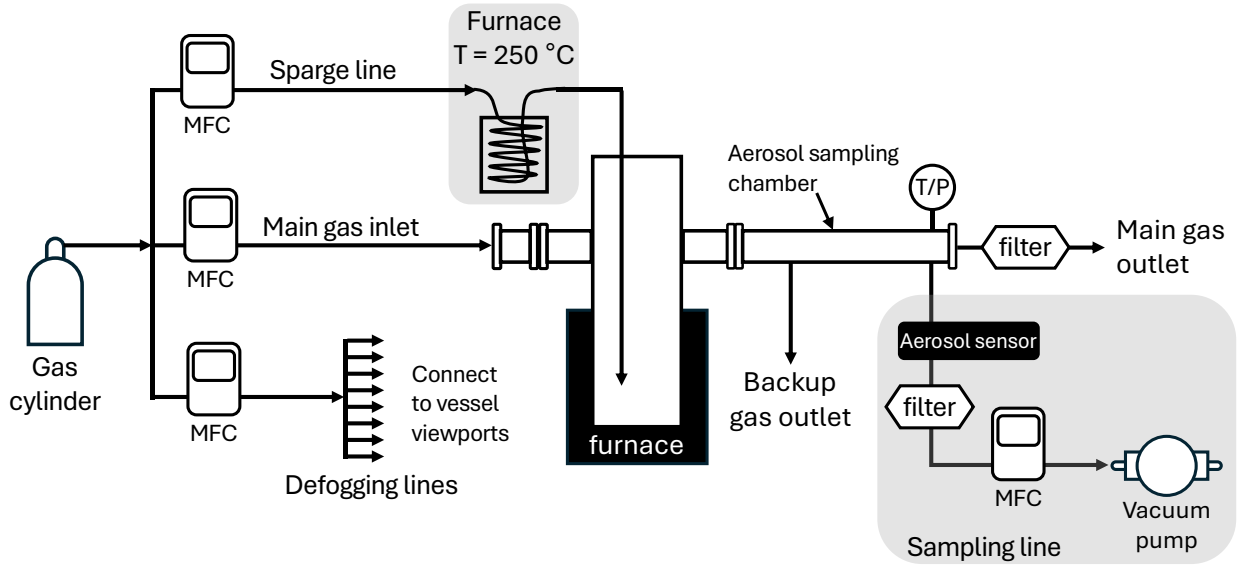

Figure 6: Simplified process and instrumentation diagram of the Argonne Salt Aerosol Test Stand

Particle detection and quantification by using the aerosol sensor is non-destructive and described in more detail in Section 2.3. The particles in the gas stream that pass through the sensor cuvette are collected on a downstream PTFE filter. The filter holder can be removed from the sampling line to allow post-test analyses of the collected particles. These include gravimetric concentration determination, elemental composition determination by using inductively coupled plasma-mass spectrometry (ICP-MS), and single particle size and composition determination by using scanning electron microscopy with associated energy-dispersive X-ray spectroscopy (SEM-EDS). The filter holder can be isolated from the ambient atmosphere prior to removal from the system using valves to limit particle exposure to humidity during transport for analysis, as moisture uptake can lead to erroneous weight and particle size measurements.

2.3 Description of aerosol sensor and calibration

The aerosol spectrometer system consists of a welas® 2070 HP sensor and Promo® 2000 controller (Palas, GmbH, Karlsruhe, Germany) and uses optical light scattering to simultaneously measure the size distribution and volumetric concentration of particles in a gas stream in real time. Detailed descriptions of the operating principle of the aerosol sensor and its suitability for measuring high temperature, corrosive, and radionuclide-bearing gas streams are provided in Thomas (2024). The sensor is calibrated for the particle size measurement with polystyrene latex microspheres provided by the manufacturer prior to salt aerosol testing. These standard particles have known size, density, and refractive index. The size calibration is performed using the same measurement size range that is used during salt aerosol tests (0.2 µm to 10 µm particle diameter). Particle size calibrations can be performed at room temperature because the temperature of the gas stream does not affect the particle size measurement (Instruction Manual Promo® 2000 Series). The sensor firmware provides size distributions of particles in the test gas stream by applying a calibration curve that was developed with the monodisperse standard particles. The PDAnalyze software included with the sensor can correct for the refractive index of the test particles, if known, to provide size distributions that better represent the true physical particle size.

The sensor obtains instantaneous volumetric particle concentration (C_V, particles cm^{-3}) from the measured rate of counted particles flowing through the measurement volume ($\dot{N}$, particles per second) and the volumetric flow rate of the carrier gas through the measurement volume (Q_V, cm^3 s^{-1}) according to Equation 1:

$$C_V = \frac{\dot{N}}{Q_V} \tag{1}$$

The velocity of the carrier gas in the measurement volume is the same as the particle velocity in the carrier gas; the sensor obtains this velocity in real time by measuring the duration of scattered light signals from individual particles within the measurement volume of known length. The Q_V under the specific conditions of the measurement is calculated from the measured particle velocity (v, cm s^{-1}) and the width (w, cm) and depth (d, cm) of the measurement volume within the sensor cuvette according to Equation 2:

$$Q_V = v \cdot w \cdot d \tag{2}$$

All particle size and concentration measurements are made using a constant carrier gas mass flow rate through the sampling line and sensor cuvette (sensor is compatible with 0.5 SLPM or 5 SLPM). When mass flow rate is held constant, the volumetric flow rate of the carrier gas depends on its temperature and pressure due to the compressibility of ideal gases. For this reason, the sensor must be calibrated for the volumetric particle concentration measurement under the same conditions as the intended measurement conditions (carrier gas temperature, pressure, and mass flow rate). This concentration calibration was done for salt aerosol tests using the generated salt particles themselves prior to the actual measurement. The quantitative accuracy of the particle size distribution measurement and volumetric particle concentration measurement using different carrier gases at different temperatures was demonstrated previously (Thomas, 2024).

3 Results

3.1 Description of tests

Eutectic LiCl-KCl was purchased from Sigma-Alrich (AnhydroBeads™, 99.99% trace metals basis) and was used for all tests. The salt was stored in ampules under inert atmosphere and opened directly before use. Prior to testing, the salt was baked out at 300 °C for 8 hours in an argon atmosphere. Eutectic LiCl-KCl was chosen as the salt composition to use to assess the formation of salt aerosols from static and sparged salt because its thermophysical and thermochemical properties are well-characterized. In addition, eutectic LiCl-KCl was a practical choice to test the sparging technique for the first time due to the relatively low melting temperature (352 °C).

A nickel crucible within the aerosol generation vessel was loaded with approximately 100 g of eutectic LiCl-KCl at room temperature under a stream of argon gas flowing over the crucible from the inlet line to limit exposure to the humidity in the ambient air. All tests were run under an argon atmosphere with argon as the sparge gas (ultra-pure grade). The vessel was then sealed with bolts and argon gas continued to flow into the aerosol generation vessel and out the main outlet line for approximately 15 minutes to purge the air from the vessel interior. After purging, the mass flow rates of argon gas through the main inlet line and through the defogging line were both set to 2 SLPM for salt heating. When used in a test, the sparger was positioned approximately 4 inches above the salt surface during salt heating and was supplied with pre-heated gas at a flow rate of 0.2 SLPM. The salt was heated under a continuous flow of argon gas and maintained at the desired temperature for approximately an hour prior to testing. Furnace setpoints to achieve the desired

salt temperatures for testing (500 °C and 600 °C) were determined by heating the salt under the same conditions for planned tests and measuring the salt temperature using an immersed thermocouple. A thermocouple was not immersed during any tests that assessed salt aerosols.

While the salt was heating in the aerosol generation vessel, the setpoint of the heated sensor cuvette was set to 100 °C to preheat the cuvette to a temperature similar to the expected carrier gas temperature. A carrier gas temperature of 100 °C was determined from preliminary tests that were conducted without salt in the vessel. The sensor cuvette is heated to maintain the temperature of the carrier gas as it flows through the sampling line from the aerosol sampling chamber. The testing protocol was performed without any salt in the aerosol generation vessel to verify that the salt is the only source of detectable particles within the system. The surface area of melted salt in the crucible was approximately 2.8 in^2 (17.8 cm^2). The salt surface was located approximately 3 in. (8 cm) from the center of the aerosol sampling chamber (in the vertical direction) and approximately 15 in. (38 cm) from the sampling line (in the horizontal direction from center to center).

Table 1 and Table 2 provide test matrices of mass flow rates through the gas lines of the system for tests conducted with static and sparged salt, respectively. The relative location of the gas lines within the system are provided in Figure 6.

Table 1: Gas line mass flow rates (SLPM) for static salt tests (varied main gas inlet flow rates)

Test no.[a]	Salt Temp. (°C)	Measurement duration (min)	Main gas inlet	Defogging line	Sampling line	Main gas outlet
1	600	60.0	5.0	2.0	5.0	2.0
2	600	27.0	5.0	2.0	5.0	2.0
3	600	19.0	10.0	2.0	5.0	7.0
4	600	28.0	7.5	2.0	5.0	4.5
5	600	6.0	5.0	2.0	5.0	2.0

[a] Tests 2, 3, 4, and 5 were performed sequentially in the order they are presented.

Table 2: Gas line mass flow rates (SLPM) for sparged salt tests (varied sparger flow rates)

Test no.	Salt Temp. (°C)	Measurement duration (min)	Main gas inlet	Defogging line	Sparge line	Sampling line	Main gas outlet
1	500	5.0	5.0	2.0	0.0[a]	5.0	2.0
2	500	9.0	5.0	2.0	0.2	5.0	2.2
3	500	9.0	5.0	2.0	0.5	5.0	2.5
4	500	8.0	5.0	2.0	0.8	5.0	2.8
5	600	60.0	5.0	2.0	0.0[a]	5.0	2.0
6	600	12.0	5.0	2.0	0.1	5.0	2.1
7	600	24.0	5.0	2.0	0.2	5.0	2.2
8	600	19.0	5.0	2.0	0.5	5.0	2.5
9	600	19.0	5.0	2.0	0.8	5.0	2.8

[a] Tests with no sparging (static salt tests) were performed before each series of sparge tests at the same salt temperature to provide a baseline measurement

3.2 Salt aerosol results

3.2.1 Static salt

Tests were run with static salt to determine the effect of measurement duration, inlet gas flow rate, and salt temperature on real-time measurements of volumetric particle concentrations and particle size distributions (PSDs). Prior to flowing particle-bearing gas through the sampling line to initiate particle measurements, the salt was maintained at the target temperature (500 °C or 600 °C) for approximately 1 hour under a flow rate from the main gas inlet of 2 SLPM. The main gas inlet flow rate was then increased to the target flow rate and aerosols were allowed to flow through the sampling line at 5 SLPM to start real time particle characterization.

Figure 7A presents the volumetric concentration (C_V) of salt aerosol particles generated from static salt at 600 °C measured in real time during a 60-minute measurement interval. The same test was run at a molten salt temperature of 500 °C, but no aerosols were detected over the measurement duration. This is likely because the vapor pressures of salts increase exponentially with temperature; the amount of vapor generated from salt at 500 °C was likely insufficient to condense into particles of detectible size. The measured volumetric particle concentration generated from static salt at 600 °C initially decreases from a concentration of approximately 4,000 particles cm^{-3} to approximately 2,500 particles cm^{-3} at the 30-minute mark (Figure 7A). The measured volumetric particle concentration then increases to approximately 4,000 particles cm^{-3} at the end of the 60-minute measurement period, appearing to approach a steady particle concentration.

The temperature and pressure of the carrier gas in the aerosol sampling chamber that were measured simultaneously with particle concentration are provided in Figure 7B and Figure 7C, respectively. The temperature and pressure of the carrier gas affect volumetric flow rate when the mass flow rate of gas through the aerosol sensor cuvette is fixed, as governed by the ideal gas law. For this reason, the particle concentration reported on a volumetric basis depends on the temperature and pressure of the carrier gas, as described in Thomas (2024). All volumetric particle concentrations presented in this report are provided with the simultaneously measured temperature and pressure of the carrier gas. The temperature and pressure of the gas in the aerosol sampling chamber remain approximately unchanged at 100 °C and 1.11 atm, respectively, during the measurement duration (Figure 7B and Figure 7C).

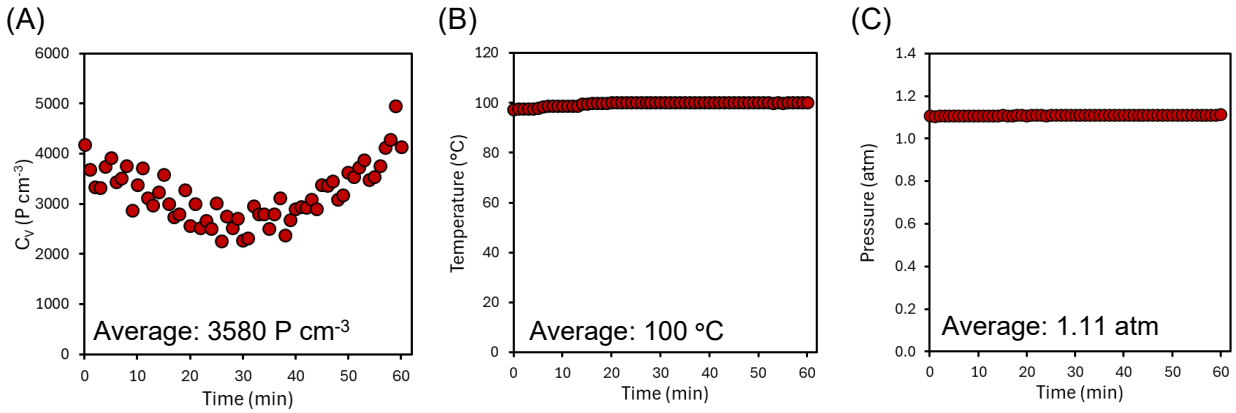

Figure 7: (A) Real-time volumetric particle concentration (C_V) of aerosol particles generated from static eutectic LiCl-KCl at 600 °C under a constant main inlet gas flow rate of 5 SLPM. (B) Temperature and (C) pressure of the carrier gas in the aerosol sampling chamber. Average values are provided in the plot windows.

Figure 8 shows salt aerosol PSDs that were averaged over 10-minute sequential measurement intervals for tests conducted with static salt at 600 °C under a constant main inlet gas flow rate of 5 SLPM. The measurement intervals are identified in each subplot in Figure 8. All PSDs presented in this report have a size resolution of 32 bins per decade (i.e., 0.1 µm to 1 µm or 1 µm to 10 µm) and are reported as the number of particles measured in a size bin divided by the total number of measured particles (dN/N or frequency). Particles with diameters greater than 0.5 µm were not detected, and bin sizes greater than 0.5 µm are not included in reported PSDs.

Pure KCl and pure LiCl have refractive indices of 1.49 and 1.66, respectively, at a wavelength of 589 nm ("Index of Refraction of Inorganic Crystals," 2023), but the refractive index of eutectic LiCl-KCl is not known. The refractive indices for the pure components are not significantly different than that of the polystyrene latex calibrant material (1.59). For this reason, the PSDs presented in this report were not corrected for refractive index and are presented as optical equivalent diameter.

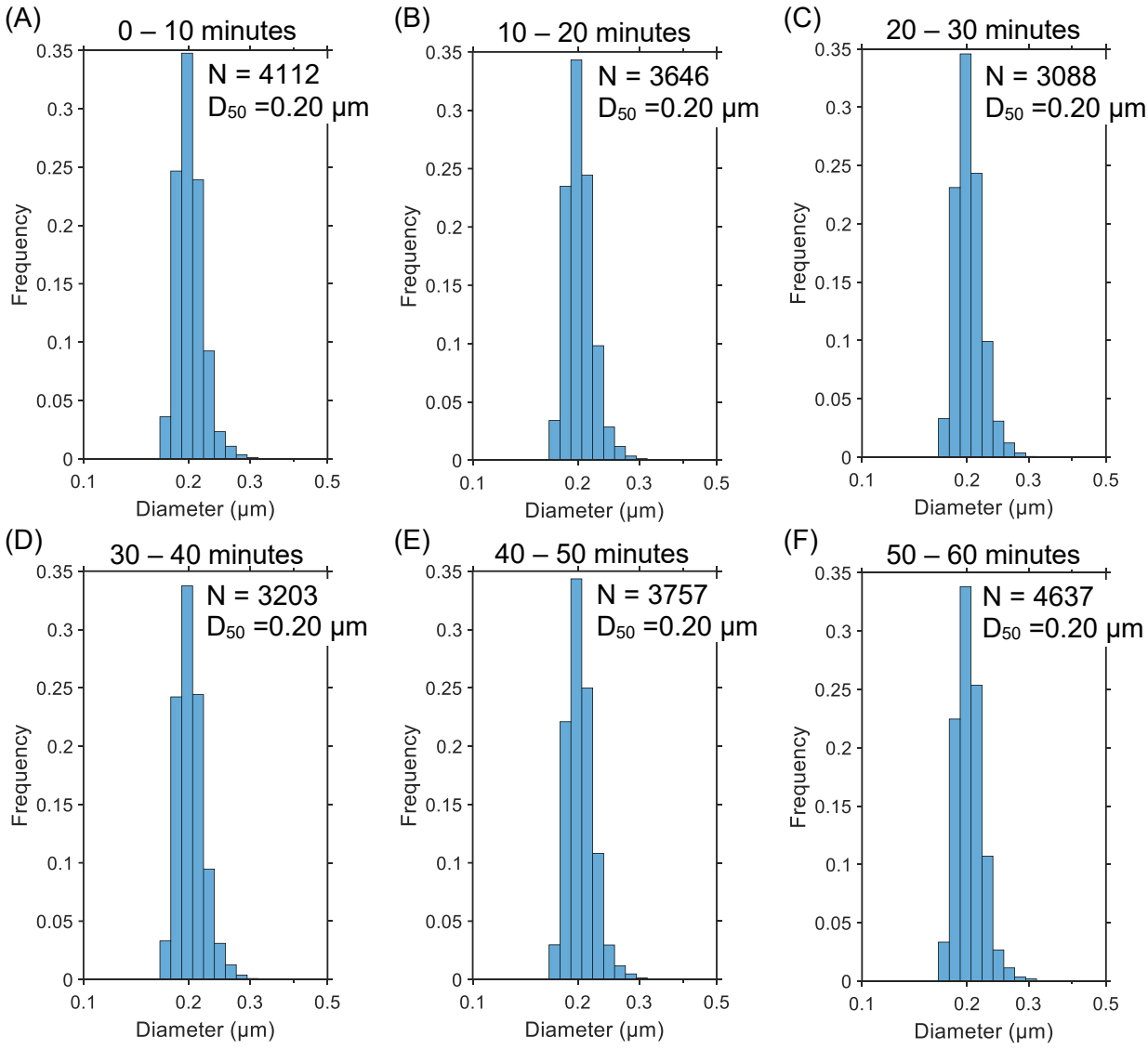

Figure 8: Average PSDs over 10-minute sequential measurement durations taken during a 60-minute test conducted with static salt at 600 °C and a main gas inlet flow rate of 5 SLPM. The D_{50} and total particles analyzed (N) for each PSD are reported in the plot windows.

Table 3 presents statistics and the total number of particles analyzed for the PSDs presented in Figure 8. Particle sizes are summarized using D_P percentiles (i.e., D_{10}, D_{16}, D_{50}, D_{84}, D_{90}), where D_P is the diameter below which p% of particles lie. The D_{50} is also known as the median particle diameter. The measured D_{50} was 0.20 µm for all conditions tested and does not change over the course of the 60-minute measurement (Table 3).

Table 3: PSD statistics from 10-minute sequential measurements during tests conducted with static salt at 600 °C under a constant main gas inlet line flow rate of 5 SLPM.

Interval number	Measurement interval (min)	Total particles analyzed	Average C_V (P cm^{-3})	D_{10}	D_{16}	D_{50}	D_{84}	D_{90}
1	0 – 10	4110	3580	0.18	0.18	0.20	0.22	0.23
2	10 – 20	3650	3180	0.18	0.18	0.20	0.22	0.23
3	20 – 30	3090	2660	0.18	0.19	0.20	0.22	0.23
4	30 – 40	3200	2660	0.18	0.18	0.20	0.22	0.23
5	40 – 50	3760	3120	0.18	0.19	0.20	0.22	0.23
6	50 – 60	4640	3910	0.18	0.19	0.20	0.22	0.23

Figure 9A presents volumetric concentrations of salt aerosols generated from static salt at 600 °C measured in real time during sequential tests at different main gas inlet flow rates that were adjusted in the following order: 5 SLPM, 10 SLPM, 7.5 SLPM, and 5 SLPM. The goal of this test series was to gain insight into how the main gas inlet flow rate affects measured particle concentration and size. The temperature and pressure of the carrier gas in the aerosol sampling chamber that were measured simultaneously with particle concentration are provided in Figure 9B and Figure 9C, respectively. Table 4 presents the average volumetric particle concentration, carrier gas temperature, and carrier gas pressure for the tests conducted under different main inlet flow rates.

The concentration of salt aerosol particles suspended in the aerosol sampling chamber at a given time during a test is a function of the aerosol generation rate from the molten salt in the vessel and the aerosol removal rate from the carrier gas due to outflow from the system through outlet lines and other processes such as deposition and coagulation. The main gas inlet flow rate can affect particle concentration in the aerosol sampling chamber because it determines the flow rate through the main gas outlet, as shown in Table 1. This means that lower inlet gas flow rates allow particles to accumulate in the aerosol sampling chamber (increased particle concentration) and higher inlet gas flow rates dilute the particle concentration in the aerosol sampling chamber (decreased particle concentration). Measured volumetric particle concentrations during the initial measurements at a main gas inlet flow rate of 5 SLPM are highest (relative to other tested inlet flow rates) because particles had accumulated in the aerosol sampling chamber during the 1-hour stabilization period prior to sampling. During the stabilization period, the main gas inlet flow rate was 2 SLPM and particles were allowed to accumulate in the system. Increasing the inlet flow rate from 5 SLPM to 10 SLPM leads to a large drop in particle concentration in the aerosol sampling chamber (Figure 9A). The measured particle concentration continues to decrease over time as flow rate is adjusted to 7.5 SLPM and stabilizes when returned to 5 SLPM. Future work should focus on developing a salt aerosol mass transport model to capture how particle generation and removal rates influence instantaneous particle concentration in the system.

The temperature and pressure of the carrier gas change in accordance with changes to the inlet gas flow rate (compare Figure 9A with Figure 9B and Figure 9C). Higher main gas inlet flow rates

yield hotter carrier gas temperatures because the inlet gas passes through the heated vessel. Higher inlet gas flow rates also produce higher pressures in the aerosol sampling chamber because the gas passes through a filter on the main gas outlet line.

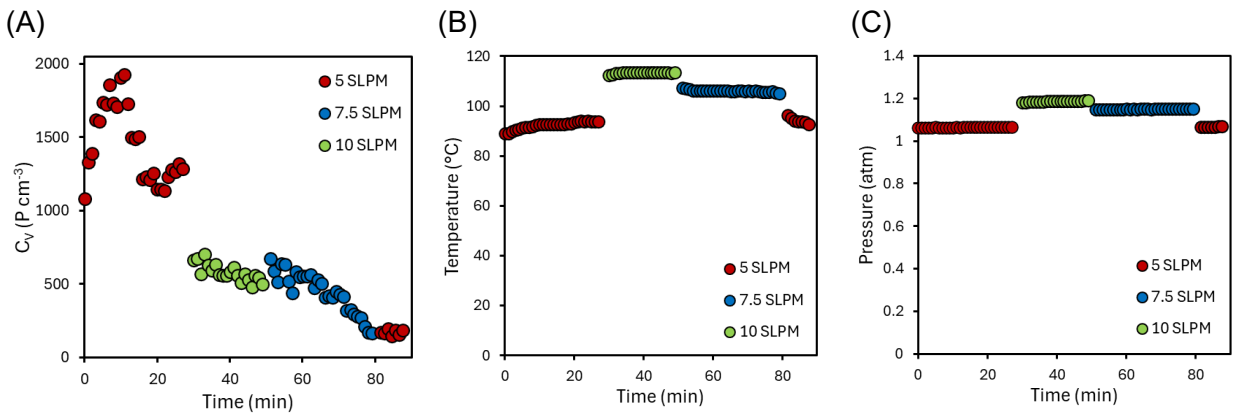

Figure 9: (A) Real-time volumetric particle concentration (C_V) of aerosol particles generated from static eutectic LiCl-KCl salt at 600 °C under different main inlet gas flow rates. (B) Temperature and (C) pressure of the carrier gas in the aerosol sampling chamber.

Table 4: Average measurements from static salt tests at 600 °C conducted with different main gas inlet line flow rates

Test	Main inlet line flow rate (SLPM)	Measurement duration (min)	Average C_V (P cm^{-3})	Average gas Temp. (°C)[a]	Average pressure (atm)[a]
1	5.0	27.0	1450	92	1.07
2	10.0	19.0	580	113	1.19
3	7.5	28.0	450	106	1.15
4	5.0	6.0	170	94	1.07

[a] In the aerosol sampling chamber directly upstream of the sampling line.

Figure 10 shows salt aerosol PSDs that were averaged over the measurement duration for tests conducted with static salt at 600 °C under different main gas inlet flow rates. Specifically, the PSDs provided in Figure 10A, Figure 10B, Figure 10C, and Figure 10D correspond to tests conducted sequentially at main gas inlet flow rates of 5 SLPM, 10 SLPM, 7.5 SLPM, and then again at 5 SLPM to show the effect of main inlet gas flow rate on particle size distribution. Particles with diameters greater than 0.5 µm were not detected, and bin sizes greater than 0.5 µm are not included in reported PSDs. Table 5 presents statistics and the total number of particles analyzed for the PSDs presented in Figure 10. The measured D_{50} was between 0.21 µm and 0.23 µm for all conditions tested and does not significantly change as a function of flow rate through the main gas inlet line (Table 5).

The results of tests conducted sequentially using different main gas inlet flow rates demonstrate how inlet gas flow rate can affect the measured particle concentrations over time by diluting or concentrating particles in the aerosol sampling chamber. A constant main gas inlet flow rate of 5 SLPM was selected as an appropriate operating condition for future tests. The inlet gas flow rate does not have nearly as significant of an effect on PSDs measured over time.

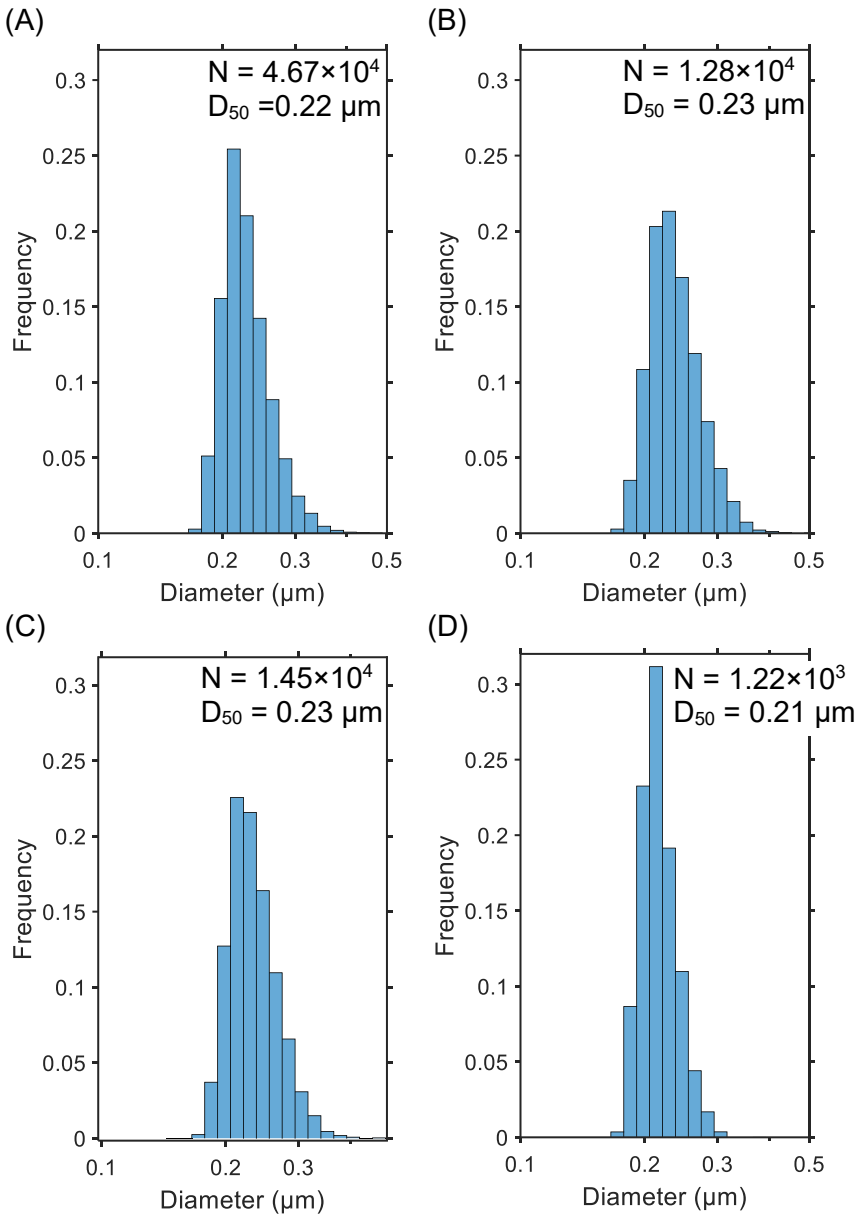

Figure 10: Average PSDs measured over the duration of each sequential test conducted using static salt at 600 °C under different main gas inlet line flow rates. The D_{50} and number of particles analyzed (N) for each PSD are reported in the plot window.

Table 5: PSD statistics for static salt tests conducted at 600 °C with different main gas inlet line flow rates.

Test	Main inlet line flow rate (SLPM)	Total particles analyzed	Average C_V (P cm^{-3})	D_{10}	D_{16}	D_{50}	D_{84}	D_{90}
1	5.0	4.67×10^4	1450	0.20	0.20	0.22	0.26	0.27
2	10.0	1.28×10^4	580	0.20	0.21	0.23	0.27	0.29
3	7.5	1.45×10^4	450	0.20	0.20	0.23	0.27	0.28
4	5.0	1.22×10^3	170	0.19	0.20	0.21	0.24	0.25

3.2.2 Sparged salt

Figure 11A and Figure 11B present real-time volumetric concentrations of salt aerosol particles generated from molten salt at 500 °C and 600 °C, respectively, when sparged with pre-heated argon gas at different mass flow rates. The tests in molten salt at temperatures of 500 °C and 600 °C began by measuring a baseline salt aerosol particle concentration from the static salt with the sparger positioned approximately 4 inches above the salt surface (out of the flow path of carrier gas flowing into the aerosol sampling chamber). The baseline measurements and the subsequent measurements for sparged salt were performed using both a main gas inlet line and sampling line flow rate of 5 SLPM (see conditions in Table 2). After completing the baseline particle concentration measurement with static salt, the sparger was immersed into the salt with sparge gas flowing at the lowest tested flow rate (0.2 SLPM for salt at 500 °C and 0.1 SLPM for salt at 600 °C). Sparging continued at a fixed mass flow rate until reaching an apparent steady particle concentration. Then, the mass flow rate of gas flowing through the sparger was increased to the next (higher) flow rate without removing the sparger from the salt. This procedure was repeated by incrementally increasing the sparger flow rate while continuously measuring real time particle concentration. A sparger mass flow rate of 1 SLPM was tested in salt at 600 °C, but the generated particle concentrations exceeded the upper detection limit of the aerosol sensor and could not reliably be measured. The sparge gas temperature (approximately 250 °C) was lower than the melting temperature of the salt (352 °C), and the effect of the sparge gas temperature on the salt temperature was not determined for this study. The sparge gas temperature is not expected to significantly affect the bulk salt temperature because the volumetric heat capacity (i.e., amount of heat required to raise the temperature of a unit volume of material by 1 K) of molten salts is orders of magnitude higher than that of gases. Video taken of the salt surface during sparging did not show any evidence of salt freezing (see Section 3.3).

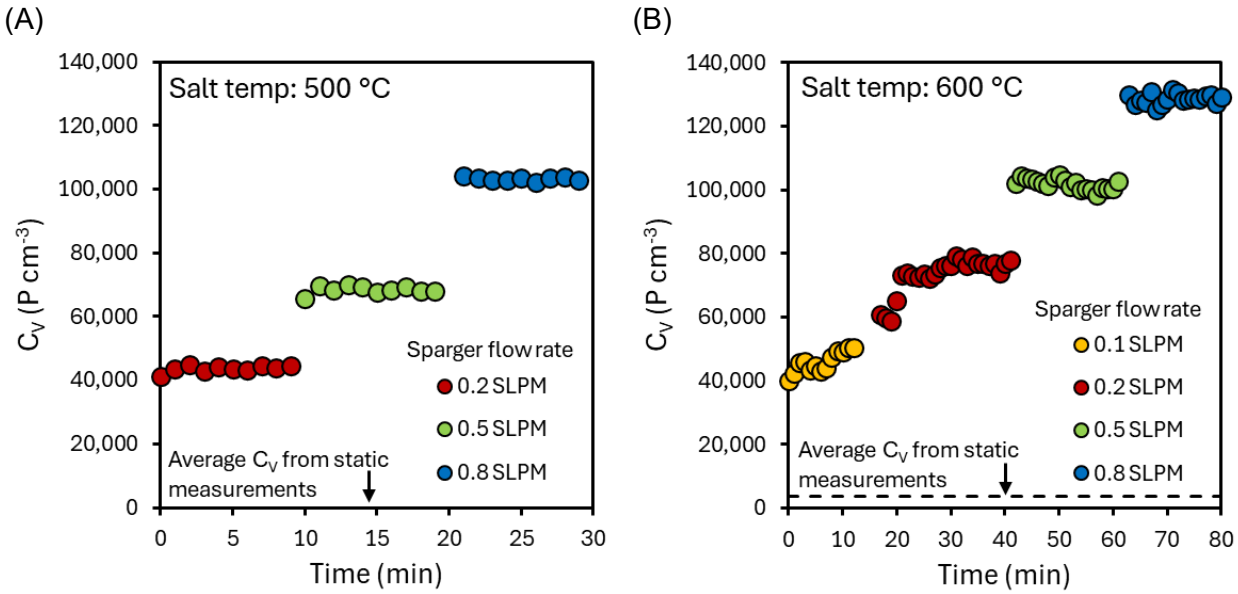

Figure 11: (A) Real-time volumetric concentration (C_V) of aerosol particles generated from salt at (A) 500 °C and (B) 600 °C that was sparged with pre-heated argon gas a different mass flow rates through a custom sparging apparatus. The baseline C_V from static salt measurements taken at the same salt temperature is represented by the dashed line (no particles were detected at 500 °C).

Figure 12 presents the temperature and pressure of the carrier gas in the aerosol sampling chamber that were measured simultaneously with particle concentration for sparge tests

performed with molten salt at 500 °C (Figure 12A and Figure 12C) and 600 °C (Figure 12B and Figure 12D). Table 6 presents the average volumetric particle concentration, carrier gas temperature, and carrier gas pressure for all sparged salt tests.

The volumetric particle concentrations measured during tests performed with sparged molten salt are significantly higher than those measured during tests performed with static salt at the same temperature (compare average C_V reported for static and sparged salts reported in Table 6). The measured volumetric particle concentration also increased with increasing gas flow rate through the sparger at each tested molten salt temperature. Notably, the measured concentrations of particles generated from sparged salt at 500 °C are lower than those generated from sparged salt at 600 °C for the same sparger flow rate (compare average C_V reported for tests with same sparger flow rate in Table 6).

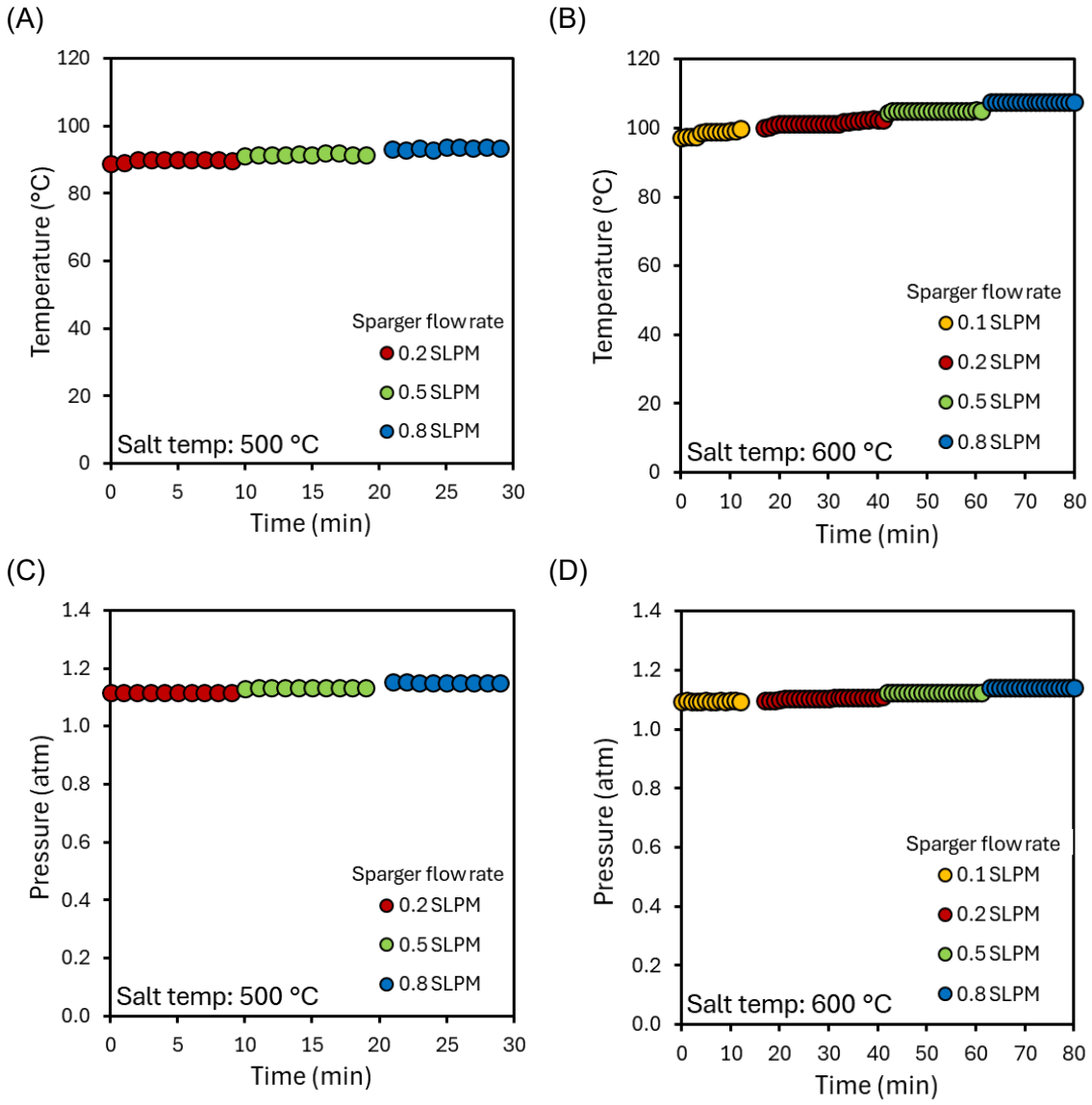

Figure 12: (A,B) Temperature and (C,D) pressure of the carrier gas in the aerosol sampling chamber during tests that sparged molten salt at (A,C) 500 °C and (B,D) 600 °C with pre-heated argon gas a different mass flow rates.

Table 6: Average measurements for tests conducted with sparged salt at different flow rates

Test no.	Salt Temp. (°C)	Sparge line flow rate (SLPM)	Measurement duration (min)	Avg. C_V (P cm^{-3})	Avg. gas temp. (°C)[b]	Avg. pressure (atm)[b]
1[a]	500	0.0 (static)	5.0	0.00	89.5	1.11
2	500	0.2	9.0	4.36×10^4	89.8	1.12
3	500	0.5	9.0	6.85×10^4	91.7	1.13
4	500	0.8	8.0	1.03×10^5	93.4	1.15
5	600	0.0 (static)	60.0	3.58×10^3	99.9	1.11
6	600	0.1	12.0	4.59×10^4	98.6	1.10
7	600	0.2	24.0	7.33×10^4	101.6	1.10
8	600	0.5	19.0	1.02×10^5	105.0	1.12
9	600	0.8	19.0	1.29×10^5	107.4	1.14

[a] No particles were detected during this test.
[b] In the aerosol sampling chamber directly upstream of the sampling line.

Figure 13 and Figure 14 present salt aerosol PSDs that were averaged over the measurement duration (i.e., duration of sparging at given flow rate) for tests conducted with sparged molten salt at a temperature of 500 °C and 600 °C, respectively. Particles with diameters greater than 0.5 µm were not detected, and bin sizes greater than 0.5 µm are not included in reported PSDs. Table 7 presents statistics and the total number of particles analyzed for the PSDs presented in Figure 13 and Figure 14. The measured D_{50} was between 0.20 µm and 0.22 µm for all sparge rates tested at both salt temperatures and does not significantly change as a function of sparge gas flow rate (Table 7).

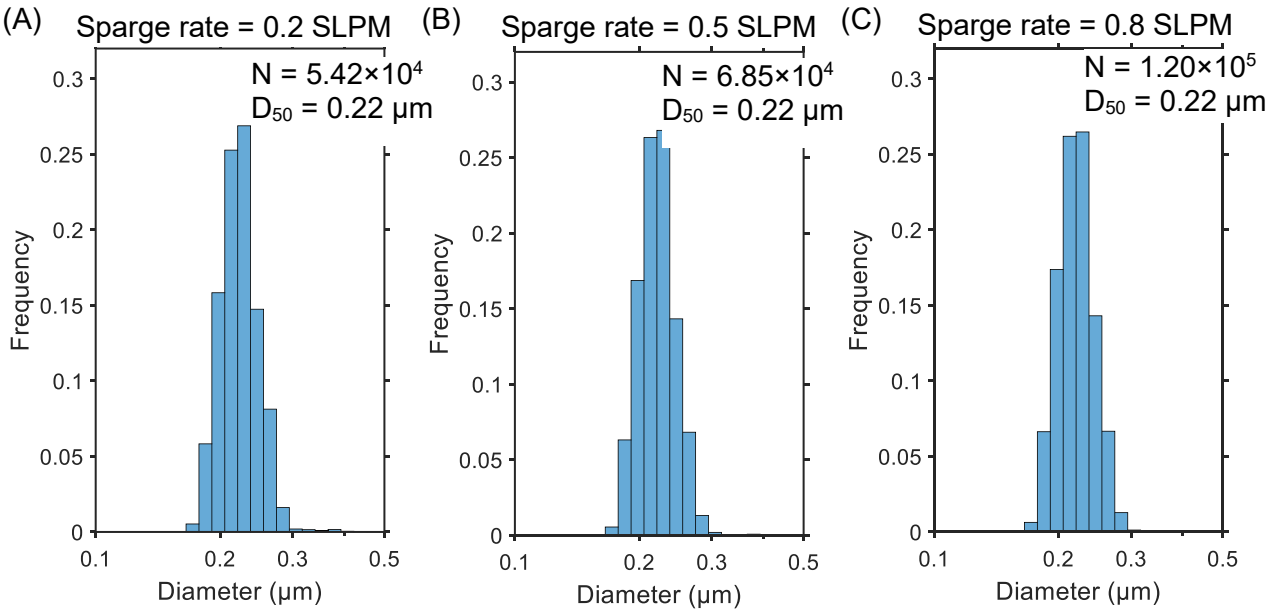

Figure 13: Average PSDs measured over the duration of each test condition for salt at 500 °C sparged with gas at flow rates of (A) 0.2 SLPM, (B) 0.5 SLPM, and (C) 0.8 SLPM. The D_{50} and number of particles analyzed (N) for each PSD are reported in the plot window.

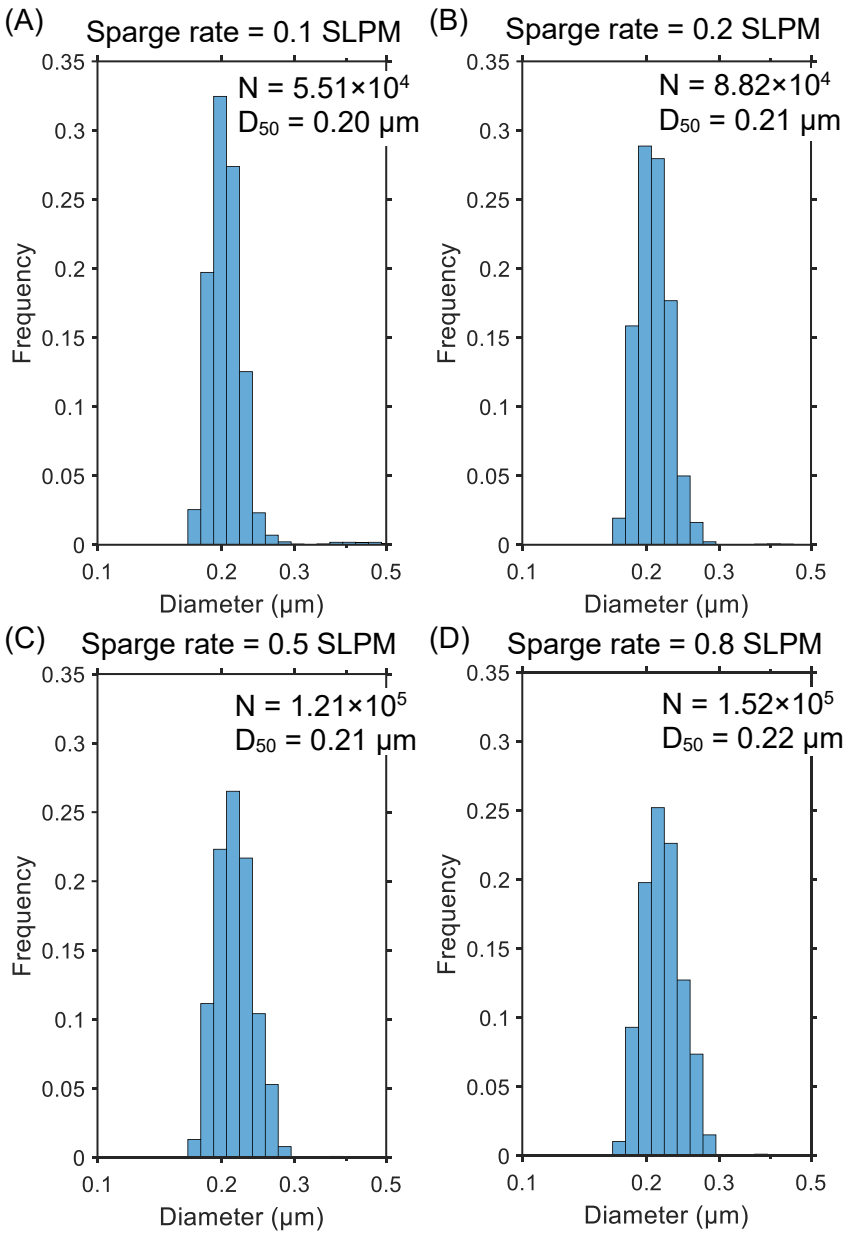

Figure 14: Average PSDs measured over the duration of each test condition for salt at 600 °C sparged with gas at flow rates of (A) 0.1 SLPM, (B) 0.2 SLPM, (C) 0.5 SLPM, and (D) 0.8 SLPM. The D_{50} and number of particles analyzed (N) for each PSD are reported in the plot window.

It is notable that the PSDs of salt aerosols generated from static salt are not significantly different from the PSDs of salt aerosols generated from salt sparged with gas at multiple flow rates. The measured volumetric particle concentrations of salt aerosols generated from sparged salts are, in general, significantly greater than those of salt aerosols generated from static salt. It is possible that the increase in measured aerosol concentration in the gas stream during salt sparging is not due to salt aerosols being mechanically formed by the bubble bursting mechanism but simply due to the increased surface area of the molten salt exposed to gas during sparging. Increased area of the salt-gas interface would increase the rate of salt vaporization and produce more salt aerosol particles generated due to the vaporization and condensation mechanism. This would explain why the measured PSDs are nearly identical when measured for both static and sparged salt at the

same temperature. This logic would also explain why higher particle concentrations were detected from sparged salt at 600 °C than from sparged salt at 500 °C for the same sparge flow rate. The presence of salt splatter on the crucible interior walls indicates that salt particles are being generated as bubbles burst during sparging. However, it is possible that these mechanically generated particles are too large to be suspended and transported in the carrier gas, such that only the small particles generated by vapor condensation reach the sensor.

Table 7: PSD statistics for tests conducted with sparged salt at 500 °C and 600 °C

Test	Salt temp. (°C)	Sparge line flow rate (SLPM)	Total particles analyzed	Avg. C_V (P cm^{-3})	D_{10}	D_{16}	D_{50}	D_{84}	D_{90}
1[a]	500	0.0 (static salt)	n.d.	n.d.	n.d.	n.d.	n.d.	n.d.	n.d.
2	500	0.2	5.42×10^4	4.36×10^4	0.19	0.20	0.22	0.25	0.26
3	500	0.5	8.28×10^4	6.85×10^4	0.19	0.20	0.22	0.25	0.25
4	500	0.8	1.20×10^5	1.03×10^5	0.19	0.20	0.22	0.25	0.25
5	600	0.0 (static salt)	2.24×10^4	3.58×10^3	0.18	0.19	0.20	0.22	0.23
6	600	0.1	5.51×10^4	4.59×10^4	0.18	0.19	0.20	0.22	0.23
7	600	0.2	8.82×10^4	7.33×10^4	0.18	0.19	0.21	0.23	0.24
8	600	0.5	1.21×10^5	1.02×10^5	0.19	0.19	0.21	0.24	0.25
9	600	0.8	1.52×10^5	1.29×10^5	0.19	0.20	0.22	0.25	0.25

[a] No particles were detected during this test (n.d. = not detected).

3.3 Surface bubble analysis

Video of the molten salt surface was recorded through the viewport windows of the aerosol generation vessel during each test. Figure 15 shows a still frame from video taken of static salt through the viewport of the aerosol generation vessel to indicate where the salt surface is located within the frame. The salt surface is located within the region where the red and blue curves intersect in Figure 15B. The view of the salt surface is partially obstructed by the viewport arm. Lighting the interior of the vessel is challenging due to the metal interior, and reflections of the lighting off the metal and salt surfaces can be observed.

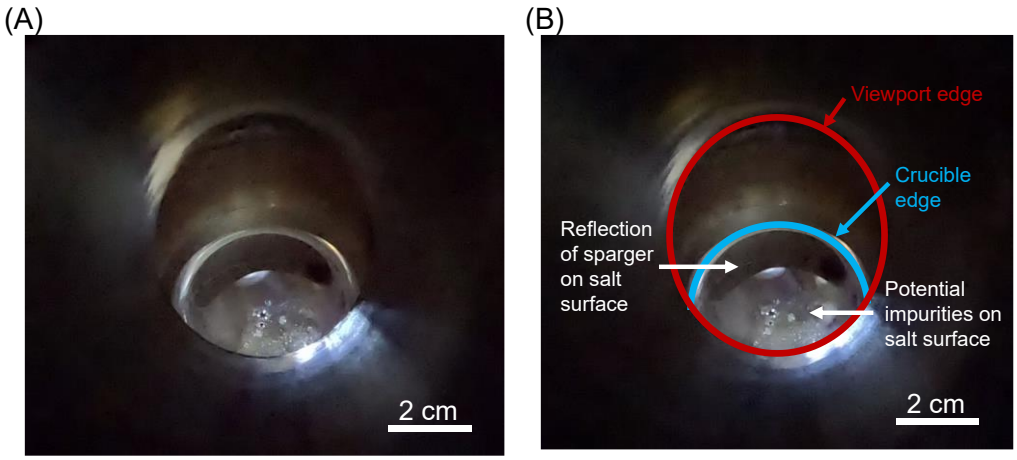

Figure 15: (A) Unannotated and (B) annotated still frame of video taken through the viewport of the aerosol generation vessel to show the static surface of salt at 600 °C. The salt surface is visible within the region where the red and blue curves intersect.

Representative still frames taken of the surface of the sparged salt at 500 °C and 600 °C are presented in Figure 16 and Figure 17, respectively. Preliminary analyses were manually performed using image analysis software to determine the sizes of bubbles present at the salt surface as a function of salt sparge rate. Pixel size was determined using objects of known dimension in the image which allowed for the approximation of bubble size. The method for surface bubble analysis is under development; trends in bubble behavior are discussed in place of quantitative analyses.

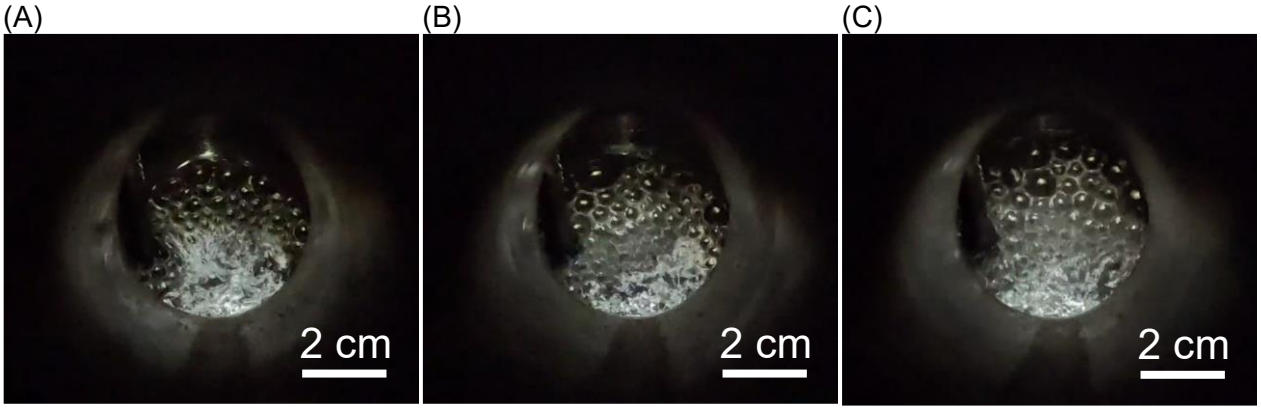

Figure 16: Still frames of video taken through a viewport of the aerosol generation vessel to show bubbles on the surface of salt at 500 °C that was sparged at a mass flow rate of (A) 0.2 SLPM, (B) 0.5 SPLM, and (C) 0.8 SLPM.

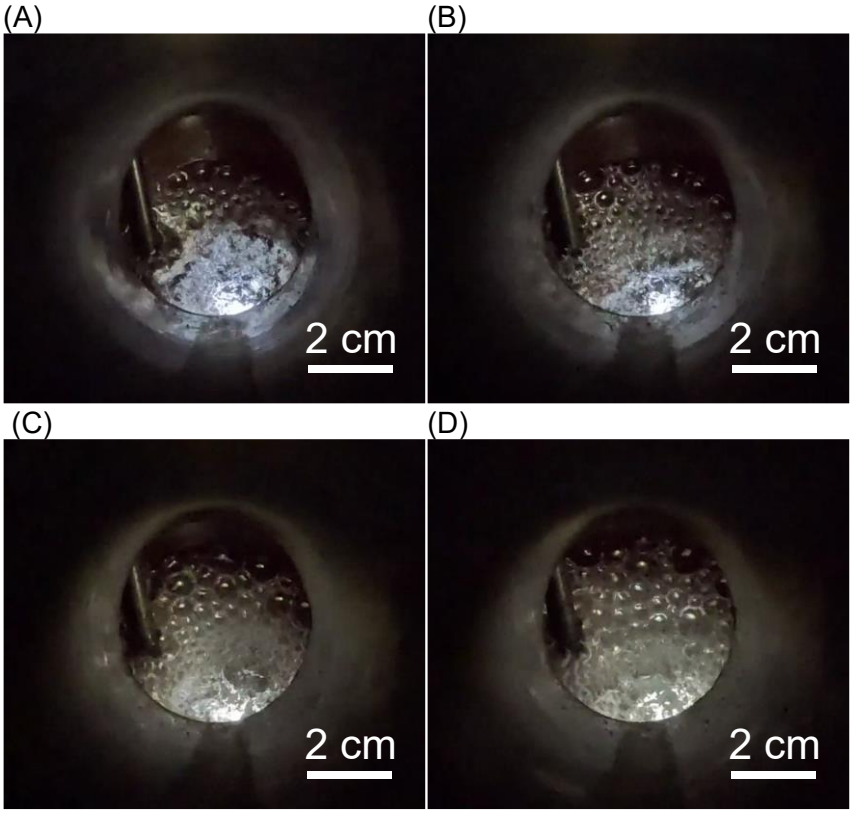

Figure 17: Still frame of video taken through a viewport of the aerosol generation vessel to show bubbles on the surface of salt at 600 °C that was sparged at a mass flow rate of (A) 0.1 SLPM, (B) 0.2 SLPM, (C) 0.5 SPLM, and (D) 0.8 SLPM.

The projected bubble diameter (i.e., diameter obtained from 2D image) measured in the images ranged from approximately 1.5 mm to as large as 7.5 mm. It is noted that the 2D projections of some bubbles are not perfect circles and the shortest dimension across the 2D projection was recorded as the diameter for irregularly-shaped bubbles. Smaller bubbles were more prevalent in images taken during tests using lower sparge flow rates and larger bubbles were more prevalent in images taken during tests using higher sparge flow rates. The higher sparge flow rates appear to produce larger bubbles due to a higher rate of coalescence (individual bubbles merging into one larger bubble). Higher sparge flow rates also lead to shorter bubble lifetimes (i.e., a higher rate of bubble bursting). Another observed trend is that the bubbles tend to move from the center of the crucible towards the crucible walls where they are more likely to coalesce; much larger bubbles are present near the crucible walls than towards the center of the crucible (Figure 16 and Figure 17). Options to improve the lighting within the aerosol generation vessel (minimize reflections off walls and salt surface) and the use of a higher quality camera will be considered for future tests to support bubble analyses.

4 Summary, applications for the data, and future work

The Argonne Salt Aerosol Test Stand was used to generate and quantify salt aerosol particles produced from static and sparged molten salt to gain insight into the characteristics of salt aerosols formed by different mechanisms. The size and concentration of salt aerosol particles were measured in real time to determine the effects of measurement duration, gas inlet flow rate, molten salt temperature, and the flow rate of the sparge gas on the produced aerosol characteristics. The major accomplishments of this work include:

- Designing and demonstrating a custom molten salt sparging apparatus that produces a lateral distribution of gas bubbles on the molten salt surface for controlled generation of salt aerosol particles from sparged salt,
- Designing a vessel with viewports and demonstrating the use of the viewports to observe the surface of molten salt contained within the vessel during the test,
- Generating salt aerosol particles from static and sparged molten salt under different controlled flow conditions to quantify the effect of bubbling on the size and concentration of these particles, and
- Recording video of the salt surface during aerosol generation tests of sparged molten salt to gain insight into surface bubble behavior, bubble size, and bubble concentration.

The major finding from this study is that sparging the molten salt significantly increases the concentration of salt aerosol particles present in the carrier gas, but the size distributions of salt aerosol particles generated from static and sparged salt are not significantly different. Sparging the molten salt with gas increases the area of the salt-gas interface, which would increase the rate of vaporization for sparged salt when compared to static salt. Thus, it is possible that the salt aerosol particles measured during tests utilizing static and sparged molten salt are primarily generated by a vapor condensation mechanism for both test conditions. Bubble bursting at the salt surface under the conditions tested may not generate salt particles that are small and buoyant enough to be transported in a gas. A general observation on surface bubble behavior for sparged salt is that salts experiencing higher sparge flow rates produced larger bubbles at the salt surface due to a higher rate of bubble coalescence. The bubbles at the surface of salts that were sparged at higher flow rates also had shorter lifetimes (i.e., higher rates of bubble bursting).

The real time measurements of salt aerosol size and concentration in this report can be used by MST and accident progression modelers (i.e., NEAMS program, MELCOR team) to develop

models that predict the characteristics of salt aerosols that form from molten fuel salt pools containing dispersed gas bubbles (e.g., generated from fission gases or sparging). The Argonne Salt Aerosol Test Stand will continue to be used to conduct separate effects tests on the characteristics of salt aerosols that form under different conditions. The results of these tests that quantify the effects of single variables will provide the mechanistic detail required to support MST modeling. The variables that will be tested in the future have relevance to normal operation and postulated accidents, including:

- **Salt composition.** Tests may be performed with both fluoride- and chloride-based salts, including those bearing actinides and surrogate fission products, to characterize the size, concentration, and composition of aerosol particles generated from these salts. Molten salts that contain separated phases (e.g., noble metals) and highly volatile salt species (e.g., CsI) may produce salt aerosol particles at sizes, concentrations, and compositions that are significantly different than those that form from salts that do not contain surrogate fission products. While the aerosol sensor described herein provides real-time measurements of particle size and concentration, complementary sampling approaches are available to measure particle composition. Particles can be collected on filters to assess the bulk elemental composition of the aerosol population or captured on carbon tape for analysis of the size and composition of individual particles. Furthermore, the non-destructive optical light-scattering technique used herein for size and concentration measurements could be integrated with a separate technique for real-time particle composition measurements such as laser-induced breakdown spectroscopy (LIBS) (Kitzhaber et al., 2025).
- **Salt and gas temperature.** Tests should be conducted using a range of salt and gas temperatures to capture thermal effects on aerosol characteristics and transport to provide insight into behaviors that may be relevant to MSRs under normal operating and accident conditions. The temperature of the molten salt affects thermophysical properties (e.g., salt density, viscosity, and surface tension) and species vapor pressure, while the temperature of the carrier gas likely influences particle formation, transport (thermophoresis), and deposition. Specialty sensor cuvettes rated for gas stream temperatures up to 450 °C can be employed to enable studies involving elevated carrier gas temperatures.
- **Presence of humidity and oxygen in the atmosphere.** Molten salts exposed to atmospheres containing humidity and oxygen are susceptible to oxidation, which can alter their thermophysical properties, speciation, and chemical reactivity. Such changes will likely influence the characteristics of aerosols generated from the salt. In addition, salt aerosol particles suspended in a gas stream containing water vapor and oxygen may change size and composition due to in situ chemical reactions and water absorption, which may affect transport behavior and particle deposition. These conditions are relevant to MSR accident scenarios involving air ingress, and their impact on salt aerosol characteristics and behavior should be systematically evaluated. This could be done by flowing oxygen-bearing gas with different levels of humidity into the aerosol generation vessel to expose the molten salt or into the aerosol sampling chamber to expose the salt particles that have already formed.
- **Particle aging, transport, and deposition.** The Argonne Salt Aerosol Test Stand can be leveraged to study salt aerosol particle behavior once the particles are formed. Specifically, salt particles can sit within the aerosol sampling chamber and be allowed to age or be exposed to different conditions (e.g., humidity, hot or cool gases). Tests may also be designed to study specific processes (e.g., thermophoresis). The existing aerosol sampling chamber could be replaced by a chamber of a different size or configuration to support these tests.

- **Static versus agitated salt.** Future tests should continue to evaluate salt aerosol formation from static and sparged salt but under conditions that incorporate added complexity. The measured sizes of particles generated from static and sparged salts were not significantly different in this study that used pure salt; however, sparging may influence salt aerosol characteristics when the source salt contains fission products or is exposed to humid or oxidizing atmospheres. Gas sparging methods could also be adapted to generate salt aerosols through mechanical processes other than by bubble bursting, for example, by producing molten salt sprays.

The method for real-time salt aerosol characterization will also be employed in future integral effects tests conducted at an engineering scale in the Salt Accident Analysis Facility (SAAF) (Thomas, 2025). These tests will simulate MSR accident scenarios involving molten fuel salt releases and may produce salt aerosol particles by additional mechanical processes that are more energetic than what is achievable in the Argonne Salt Aerosol Test Stand (i.e., by impingement of molten salt jets onto surfaces and by high velocity sprays).

References

Gelbard, F., Beeny, B. A., Humphries, L. L., Wagner, K. C., Albright, L. I., Poschmann, M., et al. (2023). "Application of MELCOR for Simulating Molten Salt Reactor Accident Source Terms." *Nuclear Science and Engineering*, 1-19.

Index of Refraction of Inorganic Crystals. (2023). In J. R. Rumble (Ed.), *CRC Handbook of Chemistry and Physics* (105 ed.).

Kitzhaber, Z. B., Orea, D., McFarlane, J., Manard, B. T., and Andrews, H. B. (2025). "Sparge Sampling of Molten Salts for Online Monitoring Via Laser-Induced Breakdown Spectroscopy." *ACS Omega, 10*(33), 37889-37897.

Shahbazi, S., Thomas, S., Kam, D. H., and Grabaskas, D. (2022). "State of Knowledge on Aerosols and Bubble Transport for Mechanistic Source Term Analysis of Molten Salt Reactors." Argonne National Laboratory Report ANL/NSE-22/47.

Thomas, S. (2024). "Method for Real-Time Salt Aerosol Concentration and Size Measurements for Molten Salt Reactor Safety Assessments." Argonne National Laboratory Report ANL/CFCT-24/25.

Thomas, S. (2025). "Preliminary Design of Engineering-Scale Salt Accident Analysis Facility to Support Molten Salt Reactor Licensing " Argonne National Laboratory Report ANL/CFCT-25/1.

Thomas, S., and Jackson, J. (2021). "Testing to Evaluate Processes Expected to Occur during MSR Salt Spill Accidents." Argonne National Laboratory Report ANL/CFCT-21/22.

Thomas, S., and Jackson, J. (2022). "MSR Salt Spill Accident Testing Using Eutectic NaCl-UCl_3." Argonne National Laboratory Report ANL/CFCT-22/32.

Thomas, S., and Jackson, J. (2023). "Intergrated Process Testing of MSR Salt Spill Accidents." Argonne National Laboratory Report ANL/CFCT-23/25.

Chemical and Fuel Cycle Technologies Division
Argonne National Laboratory
9700 South Cass Avenue, Bldg. 205

Argonne, IL 60439

www.anl.gov